Enhanced real-time power balancing of an AC microgrid through transiently coupled droop control

Manjunath Kallamadi[1] ✉, Vaskar Sarkar[1]

[1]*Department of Electrical Engineering, Indian Institute of Technology Hyderabad, India*
✉ *E-mail: kmanjunath7@gmail.com*

Abstract: The objective of this study is to improve the real-time operation of an AC microgrid for a network with high line R/X ratios. In specific, it is intended to achieve a stable microgrid operation along with accurate power sharing and minimal steady-state frequency deviation following a load disturbance. A novel droop control (DC) methodology is proposed in this regard. For a network with high line R/X ratios, there exists coupling between active power and reactive power. In existing power transformation-based approaches, the actual power sharing among different sources remains variable though both the system stability and the steady-state frequency profile can be excellent. In the DC methodology proposed, the concept of power transformation is replaced with direct power versus voltage and reactive power versus frequency droop equations. However, the active power versus voltage and reactive power versus frequency cross-couplings are taken into account only during the transient period. Therefore, the steady-state power sharing takes place in the similar manner as in the case of the normal decoupled DC. All the droop parameters are independently tuned optimising the stability performance of the system. The robustness of the proposed methodology is verified through a detailed case study.

1 Introduction

A microgrid is in effect a small-scale power system that is mainly driven by inverter interfaced renewable energy sources [1, 2]. In many cases, a microgrid is a stand-alone power system without any main grid connection. A grid-connected microgrid is also designed to run in the stand-alone mode under the circumstance of power interruption from the utility grid. Being a low inertia system, the control of a microgrid is specifically challenging for ensuring the stable system operation especially in the stand-alone mode. In one approach, the grid-forming control [3] can be adopted for a stand-alone microgrid. In the case of the grid-forming control, any one source runs in the slack mode [4], whereas all other sources run in the fixed power mode [4]. The source unit running in the slack mode is solely responsible for determining the system frequency as well as for supplying the real-time load deviations. The grid-forming control, however, lowers the system security since the loss of the slack unit leads to the complete shut-down of the microgrid. In addition, there can be inadequate power generation capacity to meet the real-time load deviations since only one source unit participates in the real-time power balancing. A conservative use of the slack unit in the dispatch scheduling, on the other hand, may lead to uneconomical operation of the microgrid. The slack unit is also supposed to have high inertia for maintaining the system stability.

To avoid all the above issues associated with the grid-forming control, the droop control (DC) of a microgrid is preferred. The DC of voltage source converters (VSCs) was originally proposed in [5]. With the DC, the real-time load deviations can be shared among all the sources according to their power ratings. This, in turn, increases the power availability to meet real-time load deviations without interfering with the dispatch scheduling. In the case of the loss of one source unit, the power sharing is completely taken over by remaining source units. The droop coefficients are usually tuned by carrying out a system level stability study [6–9]. Typically, the source frequency is drooped against its active power output, whereas the terminal voltage magnitude is drooped against the reactive power output [5–9]. Under the normal decoupled DC (DDC), the steady-state active power output of a source varies in proportion to the system frequency deviation. In the same way, the steady-state reactive power output varies in proportion to the

terminal voltage magnitude deviation. Therefore, each source has a fixed percentage share in balancing the active power to be supplied in real-time. The ratio in which the active power is shared between different sources is determined by the active power versus frequency droop coefficients. Although the reactive power sharing cannot be perfectly pre-fixed, a nearly constant ratio is maintained as long as the line voltage drop is insignificant. Instead of active power versus frequency droop, the active power versus angle droop is recommended in [10] to improve the system frequency. However, the particular approach relies on the DC power flow approximation to define the active power sharing between different sources. The DC power approximation holds good only for system with very low R/X ratio. Another way to improve the system frequency is to employ a non-linear droop relationship as was proposed in [11]. The use of non-linear droop relationship does not affect the power sharing in steady state.

The conventional DCs are based on the assumption of weak P–V and Q–δ couplings. However, the particular assumption holds true only if the following conditions are satisfied: (i) network bus voltage magnitudes are close to the nominal values, (ii) the voltage angle difference between two adjacent buses is very small and (iii) the R/X ratios of all the lines are low.

For a microgrid, the R/X ratio of a transmission line is supposed to be high since it is a low-voltage network. In the case of high R/X ratio, the bus voltage magnitudes may exhibit significant influence of the nodal active power injections. In the same way, the nodal reactive power injections are affected by bus voltage angles [12–14]. To deal with the particular issue, a power transformation technique was proposed in [15]. By performing power transformation, the droop equations are defined in terms of modified active power and modified reactive power instead of the actual active power and reactive power. Similar power transformation techniques are adopted in [16, 17]. For the work reported in [15–17], the same R/X ratio is assumed for all the lines. The concept of power transformation is extended to a system with non-uniform R/X ratios in [18, 19]. There, the different power transformations are performed for different sources depending on the R/X ratios of corresponding coupling branches.

The power transformation-based approaches suffer from the difficulty to appropriately define the power sharing among different sources. There, the power sharing is defined in terms of
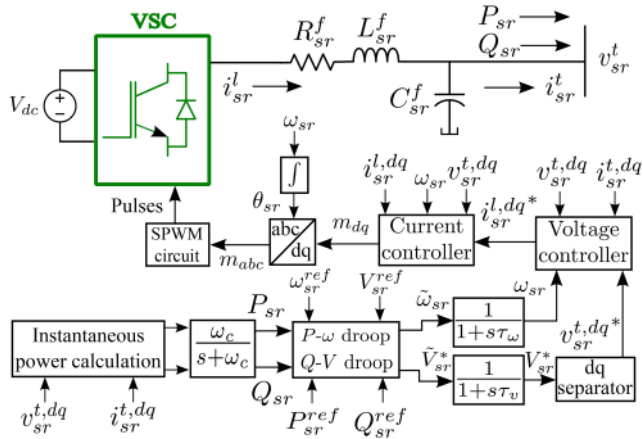
Fig. 1 *DDC control architecture*

modified active and reactive powers that are not physically significant quantities. To well maintain source operations within the corresponding ratings, the ratio of power sharing should be precisely defined in terms of the actual power quantities. In [20, 21], it is recommended to employ active power versus voltage and reactive power versus frequency droop equations for a resistive network to achieve proper power sharing. However, a clear line of demarcation between a resistive network and an inductive network in terms of the R/X ratio is not made. The consensus-based DC proposed in [22] is essentially a centralised mechanism that requires real-time co-ordination of all the sources via a fast and robust communication network. One promising approach to ensure proper sharing under high R/X ratio is to effectively reduce the R/X ratio of a transmission line through the addition of a virtual inductance in series [23, 24]. However, the virtual inductances can be added only to the coupling branches of sources. Therefore, the virtual inductance-based approach is mainly suitable when there is a point-of-common-coupling (PCC) at which all the sources are radially connected. All the remote (i.e. non-immediate loads to sources) loads should be lumped at the PCC only. The virtual inductive compensation cannot be provided to all the lines for a complex non-PCC-based microgrid configuration. In specific, the virtual inductive compensation is not available for a line that does not originate from a source bus. This, in turn, leaves the effective R/X ratio of the particular line unaltered. Thus, with virtual inductive compensations only on a few lines, it may not be possible to attain the system stability without deteriorating the system frequency. This is a similar phenomenon that can also be noted in the normal DDC.

The contribution of this paper is to propose a simple DC technique that can provide proper power sharing in a stable manner and without deteriorating the system frequency for both PCC-based and non-PCC-based microgrids. The methodology proposed is based on power transformation concept only. However, instead of performing a separate power transformation, new droop equations are incorporated to address the P–V and Q–δ couplings. In addition, those droop relationships are enforced only during the system transient. In steady state, only the standard active power versus frequency and reactive power versus voltage droop relationships define the power sharing. The linear droop equations are employed. All the droop coefficients are tuned through a system level stability study for improving the system stability to the maximum possible extent.

The remaining part of this paper is organised as follows. The basic DC, the concept of power transformation and the concept of virtual inductive compensation are reviewed in Section 2. The proposed transiently coupled DC (TCDC) methodology is explained in Section 3. In Section 4, a case study is performed to observe the performance of the proposed DC technique. Finally, this paper is concluded in Section 5.

2 Concepts of power transformation and virtual inductive compensation

For a droop-controlled source unit, the DC side of the VSC is typically represented by means of a constant voltage source. The particular representation is correct since the DC-link voltage is maintained constant by means of a battery or a battery converter. Therefore, the dynamics of source controllers (such as the MPPT controller for a photovoltaic system) on the DC side does not affect the AC side dynamics.

The control architecture of a source unit under the traditional DDC is shown in Fig. 1. The source control system is implemented in the *dq* domain. In the *dq* transformation, the q-axis is assumed to lag the d-axis and the reference frame angle is given by the angular position of the d-axis. The power invariant *dq* transformation is considered. Thus, the *dq* domain quantities can be obtained from the *abc* domain quantities through the following equation:

$$\begin{bmatrix} v_d \\ v_q \\ v_0 \end{bmatrix} = \sqrt{\frac{2}{3}} \begin{bmatrix} \cos\theta_{sr} & \cos\left(\theta_{sr} - \frac{2\pi}{3}\right) & \cos\left(\theta_{sr} + \frac{2\pi}{3}\right) \\ \sin\theta_{sr} & \sin\left(\theta_{sr} - \frac{2\pi}{3}\right) & \sin\left(\theta_{sr} + \frac{2\pi}{3}\right) \\ \frac{1}{\sqrt{2}} & \frac{1}{\sqrt{2}} & \frac{1}{\sqrt{2}} \end{bmatrix} \begin{bmatrix} v_a \\ v_b \\ v_c \end{bmatrix} \quad (1)$$

Two different instantaneous power quantities are calculated. Those are referred to as instantaneous direct power and instantaneous quadrature power. The mean of the instantaneous direct power gives the value of active power in steady state. Thus, the instantaneous direct power is, in effect, synonymous to the traditional instantaneous power. The reactive power is obtained by taking the mean of the instantaneous quadrature power in steady state. To extract the mean values of instantaneous power quantities, those are passed through low-pass filters. The filtering is specifically required when the system is unbalanced. This is because, for an unbalanced system, the instantaneous power quantities contain oscillating components. The cut-off frequency of the low-pass filters is indicated by ω_c. The outputs of the low-pass filters associated with instantaneous direct power and instantaneous quadrature power are referred to as dynamic active power and dynamic reactive power, respectively, since those are time-varying quantities during the system transient. The conventional active power and reactive power are basically the steady-state values of the dynamic active power and the dynamic reactive power, respectively. The instantaneous power calculation block calculates instantaneous direct power and instantaneous quadrature power by using the following general relationships:

$$P_{(inst)} = v_d i_d + v_q i_q \quad (2)$$

$$Q_{(inst)} = v_d i_q - v_q i_d \quad (3)$$

The output of the droop controller is governed by the following equations:

$$\tilde{\omega}_{sr} = \omega_{sr}^{ref} + d_p\left(P_{sr}^{ref} - P_{sr}\right) \quad (4)$$

$$\tilde{V}_{sr}^* = V_{sr}^{ref} + d_q\left(Q_{sr}^{ref} - Q_{sr}\right) \quad (5)$$

In the present paper, the line-to-neutral voltage magnitude [root mean square (r.m.s.)] is considered in the voltage droop equation. Symbols d_p and d_q represent the droop coefficients and the reference values set for the droop controller are indicated by 'ref' in superscripts The frequency and voltage commands generated by the droop controller are delayed through first-order delay blocks to produce the final voltage reference and frequency commands (i.e. V_{sr}^* and ω_{sr}) for the voltage controller and the source reference frame, respectively. The uses of the first-order delay blocks for generating the voltage and frequency commands are proposed in [25] for enhancing the system stability through the addition of virtual inertia. The voltage magnitude command is arbitrarily decomposed into *dq* reference values (symbolised as $v_{sr}^{t,dq*}$) by means of the *dq* separator [4]. In this paper, the q-component of the
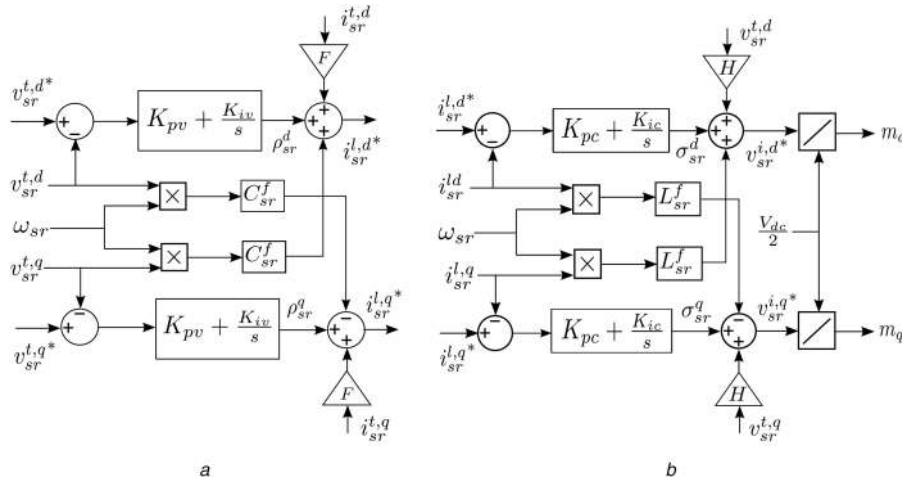
Fig. 2 *Voltage and current controller block diagrams*
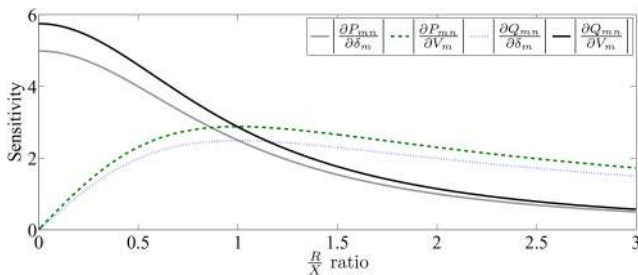*(a)* Voltage controller, *(b)* Current controller

Fig. 3 *Variation of power sensitivities with respect to voltage magnitude and angles for different line R/X ratios*

Table 1 Base voltage profile

Quantity	Base case value
V_m, V_n	1.05 pu, 0.95 pu
δ_m, δ_n	0.01 rad, 0.008 rad

transmission line reactance is taken as 0.2 pu. The base voltage profile across the transmission line is shown in Table 1.

The sensitivities of the active and reactive power flows over the transmission line to different voltage magnitude and angle quantities are observed for different R/X ratios. The line resistance is varied from 0 to 0.6 pu, so that the R/X ratio can vary from 0 to 3. The variations of power sensitivities with line R/X ratio are plotted in Fig. 3. It can be observed that for low line resistance, active and reactive powers are very little affected by voltage magnitude and angles, respectively. If both the line resistance and reactance are comparable, equal effects of voltage magnitude and angle are observed both on active power and reactive power. For very high line resistance P–V dominates the P–δ coupling and Q–δ dominates the Q–V coupling.

The objective of power transformation is to redefine the active power and reactive power, so that the DDC can be performed in terms of the modified power quantities. In general, the transformed power quantities (symbolised as P' and Q') are obtained through the following equations:

$$\begin{bmatrix} P' \\ Q' \end{bmatrix} = \begin{bmatrix} K_{pp} & -K_{pq} \\ K_{qp} & K_{qq} \end{bmatrix} \begin{bmatrix} P \\ Q \end{bmatrix} \tag{6}$$

The principle of power transformation is based on the concept of converting the original network into an equivalent network of low R/X ratio. Further explanation in this regard is provided in the Appendix. The controls of actual active power and reactive power are essentially coupled via the power transformation matrix. The source configuration with power transformation-based CDC (PTCDC) is shown in Fig. 4. In the present paper, the values of K_{pp} and K_{qq} are taken to be 1, and the values of K_{pq} and K_{qp} are set equal to the R/X ratio of the source coupling branch.

The other approach to effectively reduce the R/X ratio of a transmission line is to provide virtual inductive compensation. The virtual inductive compensation is provided by creating a virtual source terminal. A negative inductance is inserted between the actual and virtual source terminals. The negative inductance thus inserted is compensated by placing a positive inductance of equal magnitude on the other side of the virtual source terminal. This in turn reduces the R/X ratio of the coupling branch as is seen from the virtual source terminal. The concept of virtual inductive compensation is illustrated through Fig. 5a in which point RST indicates the real source terminal and point VST indicates the virtual source terminal. The active power and reactive power

dq separator output is taken to be zero (thus, $v_{sr}^{t,d*} = \sqrt{3}V_{sr}^*$). The role of the voltage controller is to maintain the *d* and *q* components of the source terminal voltage at the input reference values. The outputs of the voltage controller are the *dq* current references (symbolised as $i_{sr}^{l,dq*}$) for the current controller that is responsible for controlling the filter inductor current. The current controller generates modulation indices (symbolised m_{dq}) in the *dq* domain, which are subsequently transformed to the *abc* domain by means of the inverse *dq* transformation. The block diagrams of voltage and currents controllers are shown in Fig. 2. The further details of all the blocks can be found in [4, 7]. It is to be noted that there can be certain variations in the block diagram of a controller depending on the specific *dq* transformation employed.

The source control architecture shown in Fig. 1 is generalised enough to be applied to both unbalanced and balanced microgrids. Only the current and voltage controller architectures are shown by assuming a balanced microgrid configuration. In the case of an unbalanced microgrid, the current controller consists of two submodules for positive sequence current control and negative sequence current control [26]. In the same way, the voltage controller may comprise of two submodules. For an unbalanced microgrid, a source may be operated either in the terminal voltage balance mode or in the filter current balance mode [27]. In the first case, the negative sequence terminal voltage is maintained at zero, whereas, in the second case, the negative sequence filter current is maintained at zero. The voltage and current reference values in the submodules of voltage and current controllers are fed in accordance with the mode of control chosen.

As mentioned previously, the conventional DDC neglects the P–V and Q–δ couplings. In reality, the effect of voltage magnitude or angle on a power quantity depends on the line R/X ratio. The particular fact is illustrated through a simple example. Consider the transmission line connected between buses *m* and *n*. The terminal bus voltages of the particular line are represented by $V_m\angle\delta_m$ and $V_n\angle\delta_n$. The shunt capacitances are ignored since a microgrid network consists of only very short transmission lines. The
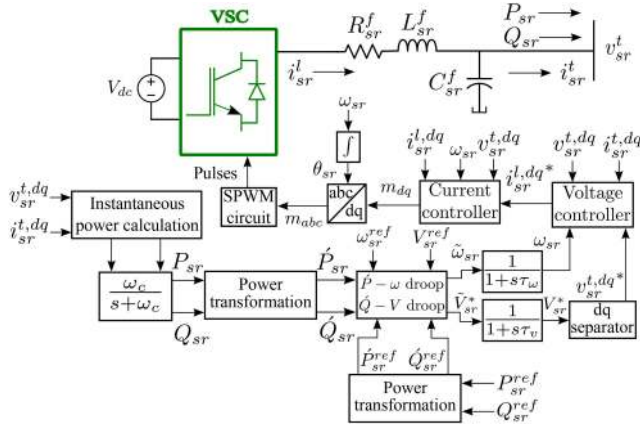
Fig. 4 *PTCDC control architecture*
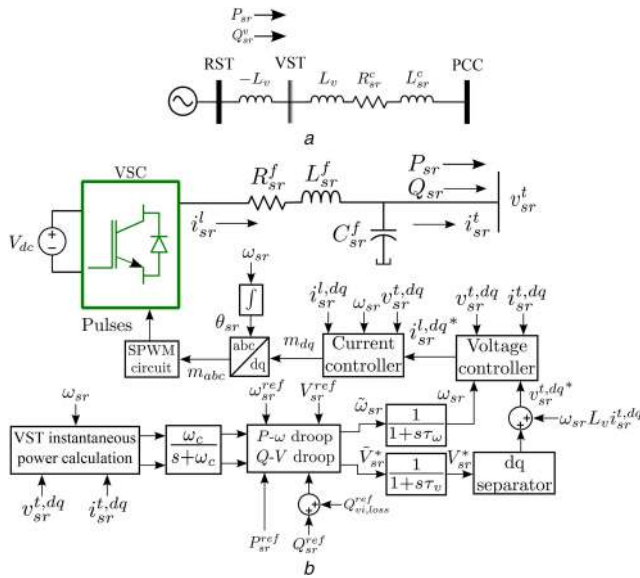

Fig. 5 *Concept of virtual inductive compensation*
(a) Schematic representation, *(b)* Control architecture

controls are kept decoupled by providing virtual inductive compensation. However, the reactive power DC is applied with respect to the voltage and reactive power output at the virtual source terminal only. The voltage drop occurring in the negative inductance between the virtual and actual source terminals is to be compensated to generate voltage references for the voltage controller, since the voltage controller is responsible for controlling the filter capacitor voltage. The source configuration with virtual inductor-based DDC (VIDDC) is shown in Fig. 5*b*. Here, the VST instantaneous power calculation block calculates the instantaneous source power outputs at the virtual source terminal. The instantaneous direct power output is calculated via the same equation as is shown in (2). However, the equation for calculating the instantaneous quadrature power is modified as follows:

$$Q_{(\text{inst})}^v = v_d i_q - v_q i_d + \omega L_v \big(i_d^2 + i_q^2 \big) \tag{7}$$

Symbols L_v and $Q_{vi,\text{loss}}^{\text{ref}}$ indicate the virtual inductance value and the reference value of the reactive power loss in the virtual inductance, respectively. The voltage reference command provided to the droop controller corresponds to the virtual terminal only. It is to be noted that the active power sharing is perfectly accurate in the case of VIDDC.

3 Proposed DC

The power transformation-based DC is basically an indirect approach for recognising P–V and Q–δ coupling effects. The PTCDC equations can be rewritten as follows:

$$\tilde{\omega}_{\text{sr}} = \tilde{\omega}_{\text{sr},\,p} + \tilde{\omega}_{\text{sr},\,q} \tag{8}$$

$$\tilde{V}_{\text{sr}}^* = \tilde{V}_{\text{sr},\,p}^* + \tilde{V}_{\text{sr},\,q}^* \tag{9}$$

where

$$\tilde{\omega}_{\text{sr},\,p} = \omega_{\text{sr}}^{\text{ref}} + \underbrace{d_p K_{pp}}_{d_{pp}} \big(P_{\text{sr}}^{\text{ref}} - P_{\text{sr}} \big) \tag{10}$$

$$\tilde{\omega}_{\text{sr},\,q} = \underbrace{-d_p K_{pq}}_{d_{pq}} \big(Q_{\text{sr}}^{\text{ref}} - Q_{\text{sr}} \big) \tag{11}$$

$$\tilde{V}_{\text{sr},\,p}^* = \underbrace{d_q K_{qp}}_{d_{qp}} \big(P_{\text{sr}}^{\text{ref}} - P_{\text{sr}} \big) \tag{12}$$

$$\tilde{V}_{\text{sr},\,q}^* = V_{\text{sr}}^{\text{ref}} + \underbrace{d_q K_{qq}}_{d_{qq}} \big(Q_{\text{sr}}^{\text{ref}} - Q_{\text{sr}} \big) \tag{13}$$

Equations (10) and (13) are the conventional active power versus frequency and reactive power versus voltage droop equations. The reactive power versus frequency and active power versus voltage droops are enforced through (11) and (12). In the case of the PTCDC, the d_{pq}/d_{pp} and d_{qp}/d_{qq} ratios are essentially set fixed. Alternatively, all the above four droop coefficients can be tuned independently.

Instead of processing $\tilde{\omega}_{\text{sr},\,p}$ and $\tilde{\omega}_{\text{sr},\,q}$ (or $\tilde{V}_{\text{sr},\,p}^*$ and $\tilde{V}_{\text{sr},\,q}^*$) in the same manner (i.e. through the same delay block), those can be processed independently. The same is the foundation for the proposed TCDC. While $\tilde{\omega}_{\text{sr},\,p}$ and $\tilde{V}_{\text{sr},\,q}^*$ are still passed through first-order delay blocks, $\tilde{\omega}_{\text{sr},\,q}$ and $\tilde{V}_{\text{sr},\,p}^*$ can be passed through wash-out filters. The source configuration with the proposed TCDC is shown in Fig. 6*a*. Since the output of the wash-out filter is always zero in steady-state, the final power sharing takes place according to active power versus frequency and reactive power versus voltage droop equations only. However, the active power versus voltage and reactive power versus frequency droops remain active during the system transient. Irrespective of whether the microgrid is balanced or unbalanced, the frequency and dynamic active power (as well as the dynamic reactive power) output of a source should settle down to constant values in steady state. As a result, in steady state, the outputs of the wash-out blocks become zero and the outputs of first-order delay blocks become equal to the respective inputs. In furtherance, the source frequencies must be equal to one another and should lead to a common system frequency (symbolised as ω_{sys}) in the steady-state. The frequency references of all the sources are usually set at the nominal system frequency (symbolised as ω_n). By symbolising the steady state through 'ss' in superscripts, the steady-state relationships between frequency and power outputs for the ith source can thus be expressed as follows:

$$\frac{1}{d_{pp,\,i}} \underbrace{\big(\omega_{\text{sys}} - \omega_n \big)}_{\Delta \omega} = - \underbrace{\big(P_{\text{sr},\,i}^{\text{ss}} - P_{\text{sr},\,i}^{\text{ref}} \big)}_{\Delta P_{\text{sr},\,i}^{\text{ss}}} \tag{14}$$

Therefore

$$\Delta P_{\text{sr},\,1}^{\text{ss}} : \Delta P_{\text{sr},\,2}^{\text{ss}} : \ldots \Delta P_{\text{sr},\,N_{\text{sr}}}^{\text{ss}} = \left(\frac{1}{d_{pp,\,1}} \right) : \left(\frac{1}{d_{pp,\,2}} \right) : \ldots : \left(\frac{1}{d_{pp,\,N_{\text{sr}}}} \right) \tag{15}$$

Here, N_{sr} indicates the number of sources in the system. Clearly, as in the case of the traditional DDC, the final active power sharing takes place precisely according to the active power versus frequency droop coefficients. The reactive power sharing also takes place similarly to that in the traditional DDC for the given reactive power versus voltage droop coefficient. The active
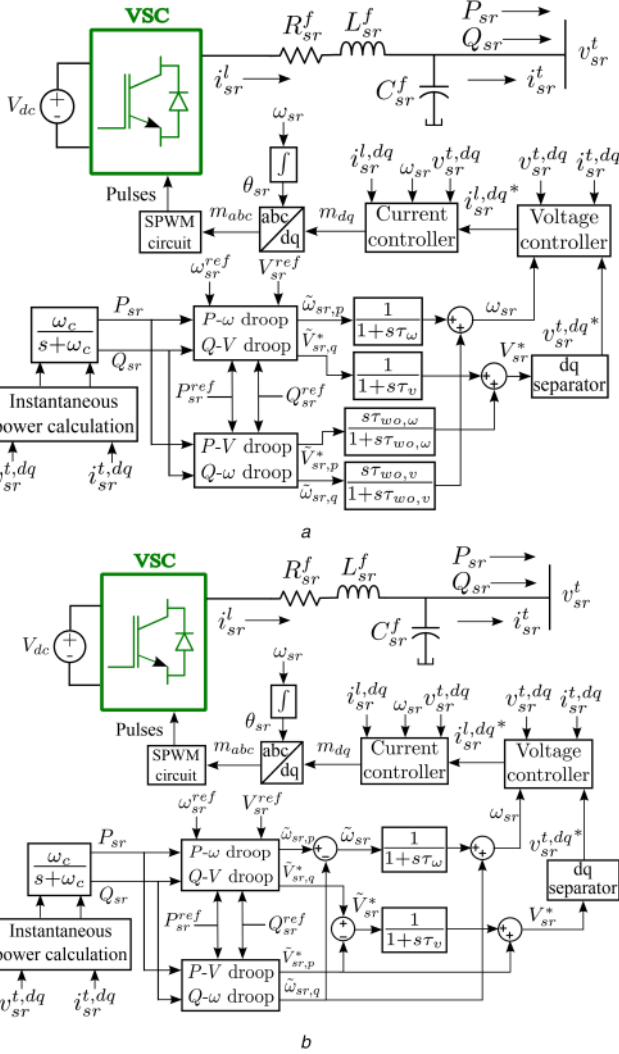
Fig. 6 *Source configuration with the proposed TCDC*
(a) Schematic representation of TCDC, *(b)* Equivalent representation of TCDC with minimum states

Fig. 7 *Single-line diagram of the test system*

Table 2 Source data

Source id.	Parameter	Value
S_1, S_3	power rating	20 kVA
	filter resistance	0.295 Ω
	filter inductance	1.47441 mH
	filter capacitance	429.5 µF
	P gain of voltage controller	0.2 Ω^{-1}
	I gain of voltage controller	9.68 $\Omega^{-1}\text{s}^{-1}$
	P gain of current controller	1.47441 Ω
	I gain of current controller	295.8 Ω/s
	cut-off frequency of low-pass filter	31.41 rad/s
S_2	power rating	10 kVA
	filter resistance	0.1 Ω
	filter inductance	1.35 mH
	filter capacitance	50 µF
	P gain of voltage controller	0.05 Ω^{-1}
	I gain of voltage controller	390 $\Omega^{-1}\text{s}^{-1}$
	P gain of current controller	10.5 Ω
	I gain of current controller	16,000 Ω/s
	cut-off frequency of low-pass filter	31.41 rad/s

Table 3 Line data

Line id.	Resistance, Ω	Inductance, H	*R/X* ratio
line 1	0.4	0.0005	2.5465
line 2	0.3	0.0008	1.1937
line 3	0.45	0.0005	2.8648
line 4	0.22	0.000636	1.1000
line 5	0.2	0.000636	1.0000
line 6	0.25	0.000636	1.2500
line 7	0.2	0.0003	2.1221

power versus voltage and reactive power versus frequency droops remain active only during the system transient.

The time constant of a wash-out filter can be taken to be equal to that of the corresponding first-order delay block (i.e. $\tau_{wo,\,\omega} = \tau_\omega$ and $\tau_{wo,\,v} = \tau_v$). In that case, TCDC system can be implemented in a simplified form as is shown in Fig. 6*b*. This will in turn eliminate the extra state variables from the source control mechanisms.

4 Case study

The case study is performed on the test system as shown in Fig. 7. The particular system consists of three sources, three induction motor (IM) loads, two power electronic loads (PELs), four thermostatic (TH) loads, three RL loads and three R loads over a 6-bus and 7-line network. The nominal voltage and nominal system frequency are 400 V (L–L) and 50 Hz, respectively. Here, acronyms 'IM', 'TH' and 'PEL' stand for induction motor load, thermostatic load and PEL, respectively. The dynamic models of TH and IM loads are obtained from [28, 29], respectively. The basic PEL configuration is taken from [9]. However, the DC-link voltage controller is chosen according to Yazdani and Iravani [4] for the convenience in its parameter tuning. In addition, the phase-locked loop (PLL) is placed across the filter capacitor terminal for the purpose of better stability and modelling convenience. The block diagram of the PLL used can be found in [30]. All the dynamic models are appropriately corrected based on the chosen *dq* transformation matrix. The detailed source, network, load data is provided in Tables 2–4.
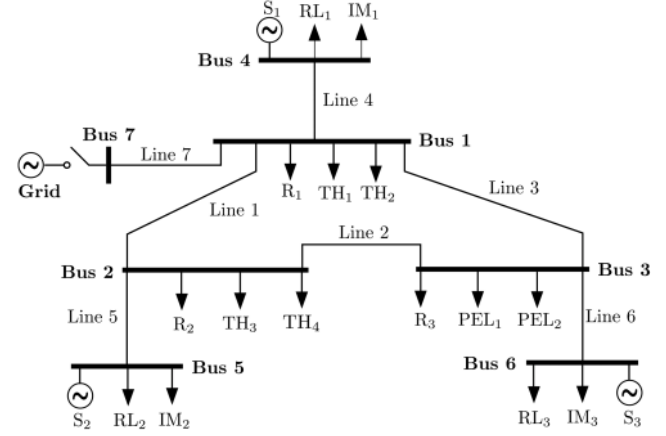
The test system in Fig. 7 is derived by modifying the system considered in [7]. The following modifications are made to represent a more realistic microgrid configuration: (i) in view of evidences of weakly meshed distribution networks in the literature [31], one new line is added to create a loop in the microgrid network; (ii) the diversity of line *R/X* ratios is maintained within a moderate range as per the power transformation theory discussed in the Appendix; (iii) the line *R/X* ratios are chosen within the range of the IEEE standard 13-bus distribution feeder [32]; and (iv) since it is often reported in the literature that the load dynamics can adversely affect the microgrid stability [13, 14], a complex load configuration is considered.

However, since it is extremely time-consuming to carry out the dynamic simulations of a large microgrid system [8], only a small-sized microgrid could be considered in the present case study. Furthermore, till date, no small-signal stability analysis

Table 4 Load data

Load id.	Parameter	Value
R_1, R_2	resistance	40 Ω, 50 Ω
R_3		40 Ω
RL_1	resistance	400 Ω
	inductance	0.6 H
RL_2	resistance	300 Ω
	inductance	0.5 H
RL_3	resistance	500 Ω
	inductance	0.4 H
IM_1, IM_2, IM_3	stator resistance	1.405 Ω
	stator inductance	0.005839 H
	mutual inductance	0.1722 H
	rotor resistance referred to stator side	1.395 Ω
	rotor inductance referred to stator side	0.005839 H
	number of poles	4
	moment of inertia	0.0131 kg m^2
	load torque (IM_1)	4.59169 Nm
	load torque (IM_2)	2.29584 Nm
	load torque (IM_3)	5.510028 Nm
PEL_1, PEL_2	coupling resistance	0.1 Ω
	coupling inductance	0.0001 H
	filter resistance	0.295 Ω
	filter inductance	1.47441 mH
	filter capacitance	429.5 μF
	DC-link voltage	900 V
	P gain of DC-link controller	3.095
	I gain of DC-link controller	29.962
	P gain of current controller	1.47441 Ω
	I gain of current controller	295.8 Ω/s
	DC capacitance	0.01 F
	DC conductance	2.469 mΩ^{-1}
	time constant of PLL	1×10^{-3} s
	P gain of PLL	1.5476
	I gain of PLL	14.9814
TH_1, TH_2, TH_3, TH_4	P gain of PI controller	−0.00074
	I gain of PI controller	−2.507
	time constant of TH load	1×10^{-3} s
	gain of TH load	−0.004
	reference temperature (TH_1, TH_2)	297 K
	reference temperature (TH_3, TH_4)	295 K
	ambient temperature (TH_1)	305 K
	ambient temperature (TH_2)	305 K

Table 5 Maximum and minimum parameter limits

Parameter	Maximum limit	Minimum limit
d_{pp}, pu	0.1	0.00001
d_{pq}, pu	0	−0.1
d_{qp}, pu	0.1	0
d_{qq}, pu	0.1	0.00001
τ_ω, s	0.01	0.0001
τ_v, s	0.01	0.0001
F	1	0

of the linearised system state matrix is investigated [7, 33]. The proportional and integral (PI) gains of current and voltage controllers are locally tuned by following the procedure discussed in [4]. For the current controller, the feed-forward path gain H is set to zero.

In the system level parameter tuning, the values of all the candidate parameters are taken to be same for all the sources. The upper and lower limits set for different parameters are shown in Table 5. The droop coefficients are equated in per unit so as to make the power sharing happen according to the source kVA ratings. The per unit values of droop coefficients are obtained as follows:

$$d_{pp}(\text{pu}) = d_{pp}\frac{S_{\max}}{\omega_n} \tag{16}$$

$$d_{pq}(\text{pu}) = d_{pq}\frac{S_{\max}}{\omega_n} \tag{17}$$

$$d_{qp}(\text{pu}) = d_{qp}\frac{S_{\max}}{V_n} \tag{18}$$

$$d_{qq}(\text{pu}) = d_{qq}\frac{S_{\max}}{V_n} \tag{19}$$

Here, $S_{\max}$ indicates the kVA rating of a source. The nominal system frequency and voltage (line-to-neutral, r.m.s) are indicated by ω_n and V_n, respectively. For the droop coefficients, the lower limits must be set to some non-zero values since the power sharing becomes undefined for zero droop coefficients. To prevent significant steady-state frequency or voltage deviation (from the nominal value), some upper limit must be imposed on a droop coefficient. The upper limit on the active power versus frequency droop coefficient is taken according to the conventional power system data [34]. The same upper limit is chosen for the other droop coefficients. With regard to the feed-forward gain of the voltage controller (symbolised as F), the lower limit essentially indicates the situation in which no feed-forward signal is passed. The upper limit of the feed-forward gain is set to the mathematical value derived in [4]. The upper and lower limits on the time constants are chosen arbitrarily.

Similarly to [35], the values of the candidate parameters in the system level parameter tuning are adjusted in a way so that the largest real part among all the eigenvalues of the linearised state matrix is minimised. The optimal parameter setting is obtained through an iterative enumeration. The permissible ranges of parameter variation are gradually shrunk over iterations. In the first iteration, the original ranges as are shown in Table 5 are considered. In each iteration, an exhaustive enumeration is carried out by varying each parameter with a certain step size within the limits set for the particular iteration. For the present case study, four iterations are run. This is in effect equivalent to enumerating a parameter by dividing its original range into 10,000 intervals in the case of 10% step size and 625 intervals in the case of 20% step size.

Apart from TCDC, results are also obtained for DDC, PTCDC and VIDDC. As mentioned previously, the VIDDC methodology is

methodology is available for an unbalanced microgrid. Therefore, for the sake of simplicity and since the main concern here is to deal with high line R/X ratios, the test system considered is taken to be balanced.

The objective of the particular case study is to verify the merit of the proposed TCDC methodology over the other methodologies in terms of the overall control performance. The overall control performance is assessed by addressing both the transient and steady-state behaviours. Only the islanded mode of operation is considered. The droop equations are taken to be linear.

A system level stability study is performed to tune the following parameters: (i) all the droop coefficients, (ii) voltage controller feed-forward gain; (iii) the time constant of the frequency delay block; and (iv) the time constant of the voltage delay block.

The system level parameter tuning is carried out by preparing the small-signal model of the entire microgrid system. Subsequently, the effect of a parameter on the eigenvalue spectrum

1938

Table 6 Base case load flow result

Bus id.	Voltage magnitude, pu	Voltage angle, rad
bus 1	1	0.0047
bus 2	1	−0.0063
bus 3	1	0.0016
bus 4	1.0077	0.0235
bus 5	1.0137	−0.0084
bus 6	1.0134	0.0016
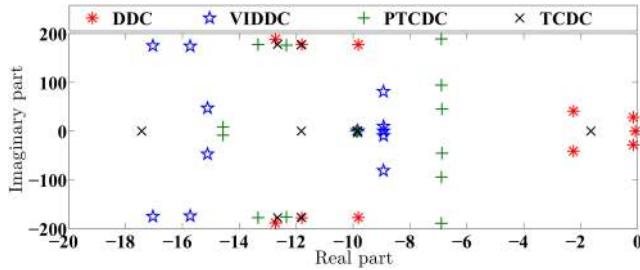
Fig. 8 *Eigenvalue spectrums for different methods*

mainly suitable for the PCC-based system. The effect of VIDDC for a non-PCC-based system is observed in this case study. The virtual inductances are inserted in a way, so that the R/X ratios of all the source coupling branches can be reduced to 0.1. In the case of DDC or PTCDC or VIDDC, only four parameters are to be tuned; therefore, the step size of parameter variation in each iteration is taken to be 10%. In contrast, six parameters are to be tuned in TCDC. To avoid the associated computational burden, the parameter variation step size is limited to only 20% in the case of TCDC. Therefore, the parameter tuning in TCDC can be somewhat less accurate compared with that in PTCDC or VIDDC.

The base case load flow result that used for the system state initialisation is shown in Table 6. From the bus voltage phasors, the line and load current phasors can be determined by using the steady-state line and load models. After the line and load current phasors are determined, the source current phasors are obtained by applying KCL at the source buses. Subsequently, the base case active and reactive power outputs of sources are determined. The base case active and reactive power outputs of sources serve as the power references in the corresponding droop controllers. The voltage reference in a droop controller is set according to the voltage magnitude at the source terminal bus (as is obtained in the load flow solution). All the frequency references are set at the nominal frequency.

From a voltage or current phasor, the initial values of DQ components (with respect to the global or common reference frame [7, 30]) of the corresponding voltage or current quantity are obtained through the following relationships:

$$\overline{V} = \frac{v_D^{(0)} - jv_Q^{(0)}}{\sqrt{3}} \qquad (20)$$

$$\overline{I} = \frac{i_D^{(0)} - ji_Q^{(0)}}{\sqrt{3}} \qquad (21)$$

Here, '(0)' in superscripts indicates the initial values. The state-space dynamics of a load element can be defined by taking the DQ components of its terminal voltage as inputs. Therefore, the initial values of load states can be easily determined by solving its state equations at the equilibrium for the given DQ components of the terminal bus voltage. Unlike loads, the source dynamics is defined in the local reference frame and by considering the terminal current as the input. It is, therefore, necessary to determine the source angle with respect to the global reference frame for converting the terminal voltage and current from globally referred quantities DQ to globally referred quantities dq. The source angle with respect to the global reference frame is directly given by the angle of the terminal bus voltage phasor. This is because the q component of

Table 7 Optimal parameter tuning results for different methods

Parameter	DDC	VIDDC	PTCDC	TCDC
d_p or d_{pp}, pu	0.0051	0.1	0.0298	0.001
d_{pq}, pu	—	—	—	−0.0262
d_{qp}, pu	—	—	—	0.0256
d_q or d_{qq}, pu	0.1	0.1	1×10^{-5}	0.0744
τ_ω, s	0.001	0.0044	0.0005	0.0001
τ_v, s	0.001	0.01	0.0005	0.0001
F	0.9424	0.6232	0.8024	0.95

the terminal bus voltage is maintained at zero in the steady state by means of the dq separator. It is to be noted that the actual source angle (i.e. θ_{sr}) does not appear in the state-space model of a source. The source state-space model is built by considering only the relative source angle with respect to the global reference frame.

The optimal parameter settings obtained for different DC methodologies are produced in Table 7. The eigenvalue spectrums under different DCs corresponding to the tuned parameter values are produced in Fig. 8. In the case of the DDC, three eigenvalues are very close to the imaginary axis indicating the possibility of poor system stability. On the other hand, the eigenvalue spectrum is significantly shifted to the left-hand side of the imaginary axis for PTCDC and VIDDC. The eigenvalue spectrum observed for TCDC is much improved compared with DDC, but is worst compared with that for PTCDC or VIDDC. However, very far shifting of the eigenvalue spectrum may not be necessary for the practical improvement of system stability.

The inference drawn from the eigenvalue analysis is further verified by carrying out a transient simulation. The transient simulation is carried out in MATLAB/Simulink with a time step of $1\,\mu$s. The original non-linear signal model of the microgrid is employed in the transient simulation. However, a VSC is represented by its averaged model. After starting the simulation at the initial steady-state, the load disturbance is added at $t = 3.5$ s by simultaneously switching off PEL$_1$ and TH$_2$ as well as by removing the load torque on IM$_1$. The dynamics of different quantities are plotted in Figs. 9 and 10. The transient performances of different DC methodologies are summarised through settling times for different quantities in Table 8. The settling time of a quantity is calculated by allowing 2% tolerance. In the case of DDC, no settling time could be calculated since the oscillations last for a very long time. For the other DC techniques, the system transient subsides within half second, which is sufficient to grade all these techniques equally from the point of view of system stability.

After investigating the system stability, the post-disturbance steady-state system condition is also studied. It can be observed that the steady-state frequency deviation is much higher in VIDDC compared with that in PTCDC or TCDC. This, in turn, makes VIDDC inferior to TCDC. Table 9 reports the power sharing (in terms of the change in power output) that takes place among different sources in steady state. In the case of TCDC and VIDDC, the active power sharing takes place precisely according to the source ratings. On the other hand, the power sharing in PTCDC does not obey source ratings. This, in turn, makes PTCDC inferior to TCDC. The system frequency profile is also found to be better in TCDC compared with that in PTCDC.

In the case of VIDDC, larger frequency deviation in steady-state happens since the active power droop coefficient is set to the upper limit in the optimal parameter tuning. Fig. 11 shows the eigenvalue and frequency dynamics plots if the optimal parameter tuning is carried out by lowering the upper limit on active power droop coefficient to 0.01. It is observable that the system stability under VIDDC is quite affected by lowering the value of the active power droop coefficient. Note that the steady-state frequency deviation is still higher than that in TCDC.
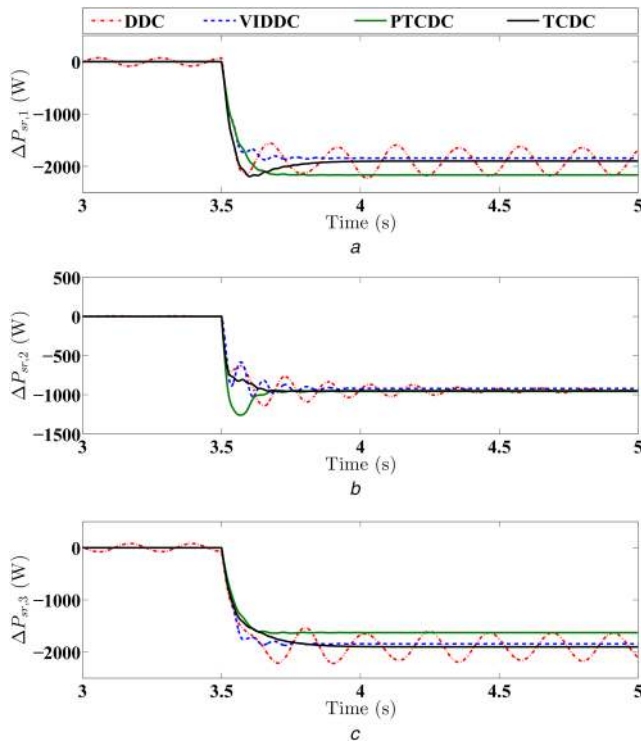
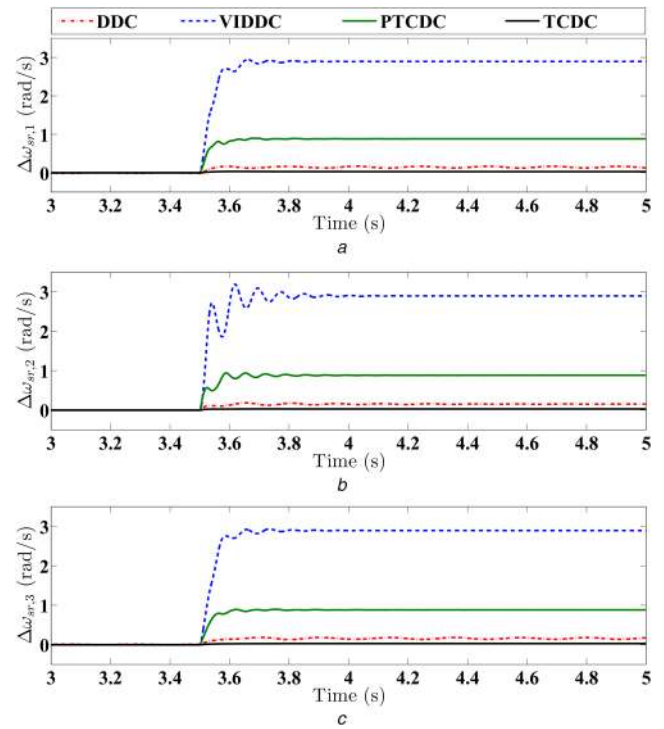**Fig. 9** *Dynamics of source active power outputs*
(a) S_1, (b) S_2, (c) S_3

Fig. 10 *Dynamics of source frequencies*
(a) S_1, (b) S_2, (c) S_3

Table 8 Settling times of different state variables for different DC methods

Source id.	State	DDC	VIDDC, s	PTCDC, s	TCDC, s
S_1	$\omega_{\text{sr, 1}}$	unsettled	0.1375	0.0901	0.3242
	$P_{\text{sr, 1}}$	unsettled	0.1328	0.1518	0.3249
S_2	$\omega_{\text{sr, 2}}$	1.3309 s	0.1671	0.1222	0.1503
	$P_{\text{sr, 2}}$	1.3303 s	0.1628	0.1021	0.1506
S_3	$\omega_{\text{sr, 3}}$	unsettled	0.1343	0.0517	0.3319
	$P_{\text{sr, 3}}$	unsettled	0.1295	0.1222	0.3328

Table 9 Steady-state active power sharings for different DC methods

Source id.	Quantity	VIDDC, %	PTCDC, %	TCDC, %
S_1	$P_{\text{sr, 1}}$	40.03	36.8	39.9
S_2	$P_{\text{sr, 2}}$	20.04	20	19.95
S_3	$P_{\text{sr, 3}}$	39.93	43.2	40.15

5 Conclusion

For a microgrid with high line R/X ratios, the traditional active power versus frequency and reactive power versus voltage droops may not provide a stable system operation without affecting the system frequency. Although the system stability can be enhanced by means of power transformation, the power sharing ratio becomes undefined. The virtual inductive compensation, on the other hand, can deteriorate the system frequency in the process of improving the system stability for a non-PCC-based system. The TCDC methodology proposed in this paper is aimed at improving the system stability along with maintaining the desired steady-state performance. Motivated by the power transformation technique, separate drooping blocks are incorporated to address the P–V and Q–δ couplings. However, the outputs of the active power versus voltage and reactive power versus frequency drooping blocks are effectively processed through wash-out filters. This in turn ensures no influence of frequency on reactive power and no influence of voltage on active power in steady state. As a consequence, the steady-state power sharing among sources remains perfectly the
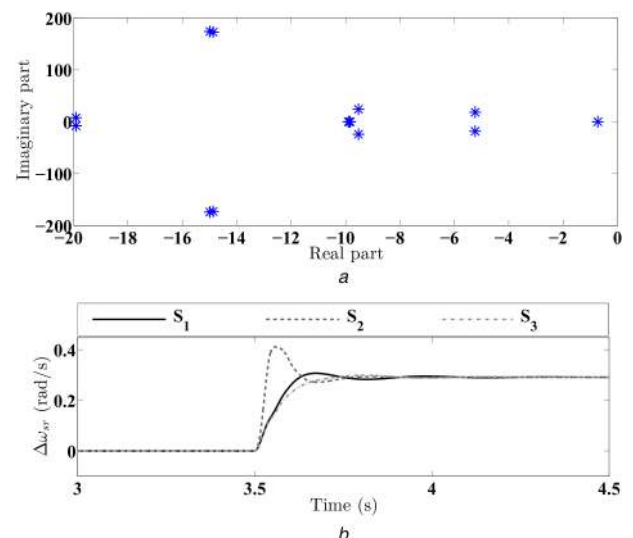

Fig. 11 *Eigenvalue and frequency dynamics plots*
(a) Eigenvalue spectrum of VIDDC with lower active power droop, *(b)* Dynamics of source frequencies for VIDDC with lower active power droop

same as that in DDC. The stability performance of the proposed TCDC methodology is verified after optimally tuning the control parameters. Compared to DDC, significant stability improvement is observed in the TCDC. The stability performances of TCDC, PTCDC and VIDDC are eventually found to be comparable. On

the other hand, the system frequency profile is found to be quite improved in TCDC compared with that in VIDDC or PTCDC.

6 References

[1] Lasseter, R.H.: 'Microgrids'. Proc. IEEE Power Engineering Society Winter Meeting, 2002, pp. 305–308

[2] Green, T.C., Prodanovic, M.: 'Control of inverter-based micro-grids', *Electr. Power Syst. Res.*, 2007, **77**, (9), pp. 1204–1213

[3] Katiraei, F., Iravani, R., Hatziargyriou, N., *et al.*: 'Microgrids management: controls and operation aspects of microgrids', *IEEE Power Energy Mag.*, 2008, pp. 54–65, doi: 10.1109/MPE.2008.918702

[4] Yazdani, A., Iravani, R.: '*Voltage-sourced converters in power systems*' (IEEE/Wiley, Piscataway, NJ, USA, 2010)

[5] Chandorkar, M.C., Divan, D.M., Adapa, R.: 'Control of parallel connected inverters in standalone AC supply systems', *IEEE Trans. Ind. Appl.*, 1993, **29**, (1), pp. 136–143

[6] Coelho, E.A.A., Cortizo, P.C., Garcia, P.F.D.: 'Small-signal stability for parallel-connected inverters in stand-alone AC supply systems', *IEEE Trans. Ind. Appl.*, 2002, **38**, (2), pp. 533–542

[7] Pogaku, N., Prodanovic, M., Green, T.C.: 'Modeling, analysis and testing of autonomous operation of an inverter-based microgrid', *IEEE Trans. Power Electron.*, 2007, **22**, (2), pp. 613–625

[8] Diaz, G., Moran, C.G., Aleixandre, J.G., *et al.*: 'Complex-valued state matrices for simple representation of large autonomous microgrids supplied by PQ and Vf generation', *IEEE Trans. Power Syst.*, 2009, **24**, (4), pp. 1720–1730

[9] Bottrell, N., Prodanovic, M., Green, T.C.: 'Dynamic stability of a microgrid with an active load', *IEEE Trans. Power Electron.*, 2013, **28**, (11), pp. 5107–5119

[10] Majumder, R., Chaudhuri, B., Ghosh, A., *et al.*: 'Improvement of stability and load sharing in an autonomous microgrid using supplementary droop control loop', *IEEE Trans. Power Syst.*, 2010, **25**, (2), pp. 796–808

[11] Rowe, C.N., Summers, T.J., Betz, R.E., *et al.*: 'Arctan power–frequency droop for improved microgrid stability', *IEEE Trans. Power Electron.*, 2013, **28**, (8), pp. 3747–3759

[12] Engler, A., Soultanis, N.: 'Droop control in LV-grids'. Proc. Int. Conf. Future Power Systems, November 2005, pp. 1–6

[13] Olivares, D.E., Mehrizi-Sani, A., Etemadi, A.H., *et al.*: 'Trends in microgrid control', *IEEE Trans. Smart Grid*, 2014, **5**, (4), pp. 1905–1919

[14] Yazdanian, M., Mehrizi-Sani, A.: 'Distributed control techniques in microgrids', *IEEE Trans. Smart Grid*, 2014, **5**, (6), pp. 2901–2909

[15] Brabandere, K.D., Bolsens, B., Keybus, J.V.D., *et al.*: 'A voltage and frequency droop control method for parallel inverters', *IEEE Trans. Power Electron.*, 2007, **22**, (4), pp. 1107–1115

[16] Majumder, R., Ledwich, G., Ghosh, A., *et al.*: 'Droop control of converter-interfaced microsources in rural distributed generation', *IEEE Trans. Power Deliv.*, 2010, **25**, (4), pp. 2768–2778

[17] Khan, H., Dasouki, S., Sreeram, V., *et al.*: 'Universal active and reactive power control of electronically interfaced distributed generation sources in virtual power plants operating in grid-connected and islanding modes', *IET Gener. Transm. Distrib.*, 2013, **7**, (8), pp. 885–897

[18] Sun, X., Tian, Y., Chen, Z.: 'Adaptive decoupled power control method for inverter connected DG', *IET Renew. Power Gener.*, 2013, **8**, (2), pp. 171–182

[19] Wu, T., Liu, Z., Liu, J., *et al.*: 'A unified virtual power decoupling method for droop-controlled parallel inverters in microgrids', *IEEE Trans. Power Electron.*, 2016, **31**, (8), pp. 5587–5603

[20] Zhong, Q.C.: 'Robust droop controller for accurate proportional load sharing among inverters operated in parallel', *IEEE Trans. Ind. Electron.*, 2013, **60**, (4), pp. 1281–1290

[21] Souza, W.F.D., Mendes, M.A.S., Lopes, L.A.C.: 'Power sharing control strategies for a three-phase microgrid in different operating condition with droop control and damping factor investigation', *IET Renew. Power Gener.*, 2015, **9**, (7), pp. 831–839

[22] Lu, L.Y., Chi, C.C.: 'Consensus-based droop control synthesis for multiple DICs in isolated micro-grids', *IEEE Trans. Power Syst.*, 2015, **30**, (5), pp. 2243–2256

[23] Tang, X., Hu, X., Li, N., *et al.*: 'A novel frequency and voltage control method for islanded microgrid based on multienergy storages', *IEEE Trans. Smart Grid*, 2016, **7**, (1), pp. 410–419

[24] Moslemi, R., Mohammadpour, J.: 'Accurate reactive power control of autonomous microgrids using an adaptive virtual inductance loop', *Electr. Power Syst. Res.*, 2015, **129**, pp. 142–149, doi: 10.1016/j.epsr.2015.08.001

[25] Liu, J., Miura, Y., Ise, T.: 'Comparison of dynamic characteristics between virtual synchronous generator and droop control in inverter-based distributed generators', *IEEE Trans. Power Electron.*, 2016, **31**, (5), pp. 3600–3611

[26] Yazdani, A., Iravani, R.: 'A unified dynamic model and control for the voltage-sourced converter under unbalanced grid conditions', *IEEE Trans. Power Deliv.*, 2006, **21**, (3), pp. 1620–1629

[27] Ju, Y., Wu, W., Zhang, B., *et al.*: 'An extension of FBS three-phase power flow for handling PV nodes in active distribution networks', *IEEE Trans. Smart Grid*, 2014, **5**, (4), pp. 1547–1555

[28] Kundur, P.: '*Power system stability and control*' (McGraw-Hill, New York, USA, 1994)

[29] Krause, P., Wasynczuk, O., Sudhoff, S.: '*Analysis of electric machinery and drive systems*' (Wiley, New Delhi, India, 2002)

[30] Kallamadi, M., Sarkar, V.: 'Generalised analytical framework for the stability studies of an AC microgrid', *IET J. Eng.*, 2016, doi: 10.1049/joe.2016.0045

[31] Kamh, M.Z., Iravani, R.: 'A sequence frame-based distributed slack bus model for energy management of active distribution networks', *IEEE Trans. Power Syst.*, 2012, **3**, (2), pp. 828–836

[32] 13-bus Feeder. Available at http://www.ewh.ieee.org/soc/pes/dsacom/testfeeders/index.html, accessed 2 December 2016

[33] Katiraei, F., Iravani, M.R., Lehn, P.W.: 'Small-signal dynamic model of a micro-grid including conventional and electronically interfaced distributed resources', *IET Gener. Transm. Distrib.*, 2007, **1**, (3), pp. 369–378

[34] Sauer, P.W., Pai, M.A.: '*Power system dynamics and stability*' (Prentice-Hall, NJ, USA, 1998)

[35] Hassan, M.A., Abido, M.A.: 'Optimal design of microgrids in autonomous and grid-connected modes using particle swarm optimization', *IEEE Trans. Power Electron.*, 2011, **26**, (3), pp. 755–767

[36] Guerrero, J.M., de Vicuna, L.G., Matas, J., *et al.*: 'Output impedance design of parallel-connected UPS inverters with wireless load-sharing control', *IEEE Trans. Ind. Electron.*, 2005, **52**, (4), pp. 1126–1135

7 Appendix

The active and reactive power flows over the transmission line *l* connected between buses *m* and *n* are given by the following equations:

$$P_{mn} = \frac{3}{X_l}\left[\frac{1}{1+\alpha_l^2}V_mV_n\sin(\delta_m-\delta_n)\right.$$
$$\left. + \frac{\alpha_l}{1+\alpha_l^2}\{V_m^2 - V_mV_n\cos(\delta_m-\delta_n)\}\right] \tag{22}$$

$$Q_{mn} = \frac{3}{X_l}\left[-\frac{\alpha_l}{1+\alpha_l^2}V_mV_n\sin(\delta_m-\delta_n)\right.$$
$$\left. + \frac{1}{1+\alpha_l^2}\{V_m^2 - V_mV_n\cos(\delta_m-\delta_n)\}\right] \tag{23}$$

Here, α_l indicates the *R/X* ratio of the *l*th transmission line. Subsequently, the equations of the modified active and reactive power flows appear as

$$P'_{mn} = \frac{3}{X_l}\left[\frac{K_{pp}+\alpha_lK_{pq}}{1+\alpha_l^2}V_mV_n\sin(\delta_m-\delta_n)\right.$$
$$\left. + \frac{\alpha_lK_{pp}-K_{pq}}{1+\alpha_l^2}\{V_m^2 - V_mV_n\cos(\delta_m-\delta_n)\}\right] \tag{24}$$

$$Q'_{mn} = \frac{3}{X_l}\left[-\frac{\alpha_lK_{qq}-K_{qp}}{1+\alpha_l^2}V_mV_n\sin(\delta_m-\delta_n)\right.$$
$$\left. + \frac{\alpha_lK_{qp}+K_{qq}}{1+\alpha_l^2}\{V_m^2 - V_mV_n\cos(\delta_m-\delta_n)\}\right] \tag{25}$$

Let

$$\left(\frac{1}{X_l}\right)\left(\frac{K_{pp}+\alpha_lK_{pq}}{1+\alpha_l^2}\right) = \left(\frac{1}{X_l}\right)\left(\frac{\alpha_lK_{qp}+K_{qq}}{1+\alpha_l^2}\right) = \left(\frac{1}{X'_l}\right)\left(\frac{1}{1+\alpha_l'^2}\right) \tag{26}$$

$$\left(\frac{1}{X_l}\right)\left(\alpha_l\frac{K_{pp}-K_{pq}}{1+\alpha_l^2}\right) = \left(\frac{1}{X_l}\right)\left(\frac{\alpha_lK_{qq}-K_{qp}}{1+\alpha_l^2}\right) = \left(\frac{1}{X'_l}\right)\left(\frac{\alpha_l'}{1+\alpha_l'^2}\right) \tag{27}$$

Therefore

$$P'_{mn} = \frac{3}{X'_l}\left[\frac{1}{1+\alpha_l'^2}V_mV_n\sin(\delta_m-\delta_n)\right.$$
$$\left. + \frac{\alpha_l'}{1+\alpha_l'^2}\{V_m^2 - V_mV_n\cos(\delta_m-\delta_n)\}\right] \tag{28}$$

$$Q'_{mn} = \frac{3}{X'_l}\left[-\frac{\alpha_l'}{1+\alpha_l'^2}V_mV_n\sin(\delta_m-\delta_n)\right.$$
$$\left. + \frac{1}{1+\alpha_l'^2}\{V_m^2 - V_mV_n\cos(\delta_m-\delta_n)\}\right] \tag{29}$$

For the relationships (26) and (27), the following conditions must be satisfied:

$$K_{pp} = K_{qq} \tag{30}$$

$$K_{pq} = K_{qp} \tag{31}$$

Finally, the solutions for α'_l and X'_l are obtained as follows:

$$\alpha'_l = \frac{\alpha_l K_{pp} - K_{pq}}{K_{pp} + \alpha_l K_{pq}} \tag{32}$$

$$X'_l = X_l \left(\frac{1 + \alpha_l^2}{1 + \alpha_l'^2} \right) \left(\frac{1}{K_{pp} + \alpha_l K_{pq}} \right) \tag{33}$$

Equations (32) and (33) show that the original system is transformed into a new system with different line reactances and ratios. The transformed power quantities in the original system represent the actual power quantities in the new system for the same bus voltage magnitudes and angles. By taking the same power transformation matrix throughout the system, the nodal power balance in terms of the modified power quantities is ensured. To ensure non-negativities of reactance and resistance in the transformed system, the following conditions should be further imposed while selecting the power transformation matrix:

$$K_{pp} \geq -\alpha_l K_{pq}, \ \forall l \tag{34}$$

$$K_{pp} \geq \left(\frac{1}{\alpha_l} \right) K_{pq}, \ \forall l \tag{35}$$

By assuming non-negative K_{pp} and K_{pq} it is sufficient to satisfy condition (34). Relationships (32), (34) and (35) together define the conditions for a valid power transformation. The value of α'_l is minimised [subjected to conditions (34) and (35)] for the following choice of K_{pp} and K_{pq}:

$$K_{pq} = \alpha_{\min} K_{pp} \tag{36}$$

Here, $\alpha_{\min}$ is the lowest R/X ratio among all the transmission lines. The value of K_{pp} is chosen as R/Z in the literature. However, the particular value can be arbitrarily chosen. This will only scale up or scale down the values of droop coefficients.

By minimising α'_l, the original system is effectively transformed to a new system with low line R/X ratios. It is, however, necessary that the original R/X ratios of different lines may not significantly differ from one another. Otherwise, the R/X ratios of certain lines in the transformed system can still be very high. As an example, let the highest and lowest line R/X ratios in a given network be 2.5 and 0.2, respectively. For the particular system, the power transformation concept may not be useful since the highest line R/X ratio that can be seen in the transformed network is 1.5333. Clearly, the success of the power transformation methodology largely depends on the diversity of line R/X ratios within a network.

In this case, the R/X ratios of all the lines in the original system are the same and the transformed system becomes purely inductive as in [15–17]. Otherwise, it is likely that the lowest R/X ratio may happen in a source coupling branch [19, 36]. By assuming close R/X ratios of all the coupling branches, the choice of a different power transformation matrix (as in [19]) for each source according to the R/X ratio of its own coupling branch should be accurate enough to fit into above concept of network transformation.